Ferrimagnetically ordered states in the Hubbard model on the hexagonal golden-mean tiling

Akihisa Koga[1] and Sam Coates[2]
[1]*Department of Physics, Tokyo Institute of Technology, Meguro, Tokyo 152-8551, Japan*
[2]*Department of Materials Science and Technology, Tokyo University of Science, Katsushika, Tokyo 125-8585, Japan*

(Received 5 January 2022; accepted 1 March 2022; published 11 March 2022)

We study magnetic properties of the half-filled Hubbard model on the two-dimensional hexagonal golden-mean tiling. We find that the vertex model of the tiling is bipartite, with a sublattice imbalance of $\sqrt{5}/(6\tau^3)$ (where τ is the golden mean), and that the noninteracting tight-binding model gives macroscopically degenerate states at $E = 0$. We clarify that each sublattice has specific types of confined states, which in turn leads to an interesting spatial pattern in the local magnetizations in the weak coupling regime. Furthermore, this allows us to analytically obtain the lower bound on the fraction of the confined states as $(\tau + 9)/(6\tau^6) \sim 0.0986$, which is conjectured to be the exact fraction. These results imply that a ferrimagnetically ordered state is realized even in the weak coupling limit. The introduction of the Coulomb interaction lifts the macroscopic degeneracy at the Fermi level and induces finite staggered magnetization as well as uniform magnetization. Likewise, the spatial distribution of the magnetizations continuously changes with increasing interaction strength. The crossover behavior in the magnetically ordered states is also addressed in terms of the perpendicular space analysis.

DOI: 10.1103/PhysRevB.105.104410

I. INTRODUCTION

Quasicrystals and their related phenomena have been of much interest since the first discovery of the quasicrystalline phase of Al-Mn [1]. Recently, intriguing low-temperature properties originating from electron correlations have been observed in quasicrystalline and approximant intermetallic phases, including quantum criticality [2,3], heavy-fermion behavior [2,3], and superconductivity [4]. Particular attention has been paid to magnetic properties in quasicrystals, with the majority of compounds showing spin-glass-like states [1,5,6–14]. However, long-range ordered states have been reported in approximant systems [15] and, recently, even in quasicrystals [16]. These novel observations rightfully stimulate further theoretical investigations on electron correlations inherent in quasicrystalline matter [17–20]. A fundamental question is how a quasiperiodic structure affects physical properties in its ordered state. Quasiperiodic tilings provide an exemplar playground for exploring the theoretical answers to this question: investigating, for example, superconducting and excitonic insulating states [21–24]. Indeed, it has been clarified that the effect of the quasiperiodic structure appears in the bulk quantities in addition to local quantities [25].

To this end, magnetically ordered states on tilings have been well studied [26–32], with interesting magnetic properties reported under the Hubbard models on the Penrose [27,29], Ammann-Beenker [28,30], and Socolar dodecagonal tilings [31]. Here, no uniform magnetization appears in the thermodynamic limit, and antiferromagnetically ordered states are always realized when the Coulomb interaction is finite. Likewise, in the weak coupling regime, spontaneous magnetization strongly depends on the distribution of the confined states, while it depends on the local environment in the strong coupling regime. These results are commonly found in the toy models on these three quasiperiodic tilings. Therefore, for broader analysis, and the potential for discovering novel properties, it is desirable to examine the magnetic properties of other quasiperiodic tilings.

In our previous paper [33], we defined the quasiperiodic hexagonal golden-mean tiling. The tiling is composed of rhombuses and parallelograms, the vertex model is bipartite, and the system has sixfold rotational symmetry, with a portion shown in Fig. 1(a). With our definition it is now possible to explore the wider properties of the tiling—with the aim of understanding and showcasing its place within the quasiperiodic tiling family. In this paper, we examine the tiling structure in detail, with a view to a discussion of its magnetic properties in the half-filled Hubbard model. First, in Sec. II, we explain the hexagonal golden-mean tiling in detail, clarifying the existence of a sublattice imbalance which is distinct from that of the Penrose, Ammann-Beenker, and Socolar dodecagonal tilings [29–31]. In Sec. III, we introduce the half-filled Hubbard model on the hexagonal tiling. Then, we study the confined states with $E = 0$ in Sec. IV, which should play an important role for magnetic properties in the weak coupling limit. We find that the confined state properties are also distinct from the above cases. Furthermore, we obtain the fraction of the confined states in terms of Lieb's theorem [34], considering the magnetism in the weak coupling limit. By means of the real-space Hartree approximations, we then clarify how a ferrimagnetically ordered state is realized in the Hubbard model in Sec. V. Finally, crossover behavior in the ordered state is addressed by mapping the spatial distribution of the magnetization to the perpendicular space.

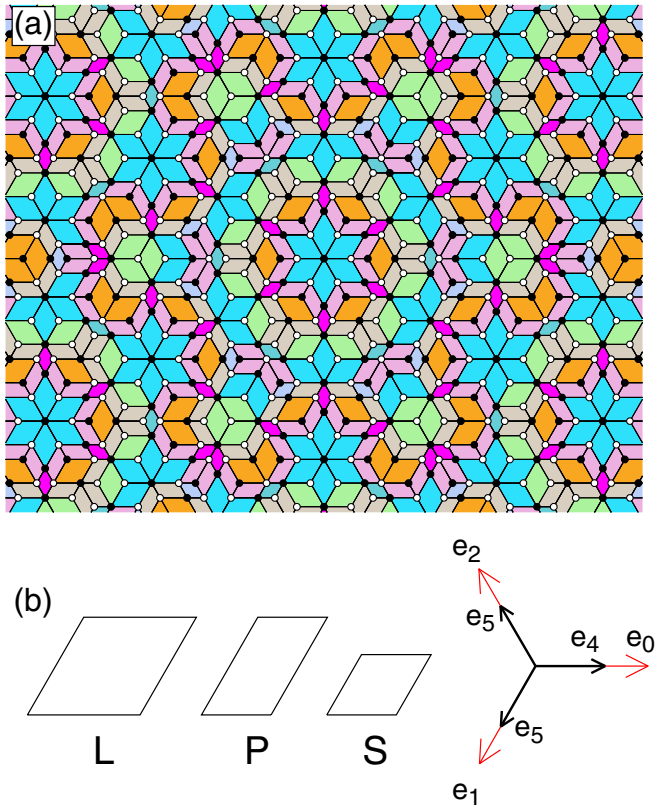

FIG. 1. (a) Hexagonal golden-mean tiling. Filled (open) circles at the vertices indicate the sublattice A (B) in the system. (b) Large rhombus, parallelogram, and small rhombus. $\mathbf{e}_0, \ldots, \mathbf{e}_5$ are the projection of the fundamental translation vectors in six dimensions, $\mathbf{n} = (1,0,0,0,0,0), \ldots, (0,0,0,0,0,1)$.

II. HEXAGONAL GOLDEN-MEAN TILING

The hexagonal golden-mean tiling is composed of large rhombuses (L), parallelograms (P), and small rhombuses (S), which are schematically shown in Fig. 1(b), where the ratio of the longer and smaller lengths of their edges is the golden ratio $\tau = (1+\sqrt{5})/2$ [33]. The tiling can be generated using grid dualization or high-dimension projection, but here, we make use of the substitution rules to generate its structure, since it is straightforward to obtain the exact fractions for various diagrams in the thermodynamic limit. In this case, the three basic tiles are further characterized by eight types of substitutions. The rules for this extended tile set are schematically shown in Fig. 2(a), where we define three large rhombuses (L1, L2, L3), two parallelograms (P1, P2), and three small rhombuses (S1, S2, S3). In this schematic we also decorate the tiles with arrows, open triangles, and open circles on their edges, to demonstrate and satisfy the matching rules we have previously defined [33]. The fractions of the tiles in the infinite tiling are given as

$$f_{\mathrm{L1}} = \frac{1}{2\tau^2} \sim 0.191, \tag{1}$$

$$f_{\mathrm{L2}} = \frac{1}{4\tau^2} \sim 0.095, \tag{2}$$

$$f_{\mathrm{L3}} = \frac{1}{4\tau^2} \sim 0.095, \tag{3}$$

$$f_{\mathrm{P1}} = \frac{1}{\tau^3} \sim 0.236, \tag{4}$$

$$f_{\mathrm{P2}} = \frac{1}{\tau^3} \sim 0.236, \tag{5}$$

$$f_{\mathrm{S1}} = \frac{1}{2\tau^4} \sim 0.073, \tag{6}$$

$$f_{\mathrm{S2}} = \frac{1}{4\tau^4} \sim 0.036, \tag{7}$$

$$f_{\mathrm{S3}} = \frac{1}{4\tau^4} \sim 0.036. \tag{8}$$

The tiling contains 32 distinct types of vertices, which are classified into four groups specified by their coordination numbers Z, with $Z = 3, 4, 5$, and 6, which we label as the C, D, E, and F vertices, respectively. Each vertex is specified by its group and an index i, as explicitly shown in Fig. 2(b). The fractions of the vertices can be obtained by examining the deflation rule [33], with these values shown in Table I. We note that the average of the coordination number is 4, which is the same for the vertex model on the Penrose and Ammann-Beenker tilings, and square lattice. Therefore one may expect that magnetic properties in the hexagonal golden-mean tiling are similar to those on the above lattices.

We note that there are some vertices with local rotational symmetry which exhibit interesting substitution behavior. For instance, the F_0 vertex is located at the center of six adjacent L1 rhombuses and thereby has local sixfold rotational symmetry. Under one substitution of its surrounding tiles [see Fig. 2(a)], we find that the F_0 vertex remains unchanged, which is behavior unique to this position. Likewise, there are four vertices with local threefold rotational symmetry, such as C_0, C_1, F_4, and F_5. According to the deflation rule, these vertices are changed in a cyclical manner as $\mathrm{C}_1 \to \mathrm{C}_0 \to \mathrm{F}_4 \to \mathrm{F}_5 \to \mathrm{C}_1 \to \cdots$. Both of these properties will be important when examining the number of confined states in the tiling.

Now we consider the sublattice structure in the hexagonal golden-mean tiling, which is important for discussing magnetic properties in the Hubbard model. To do so, we first must introduce a "spin" for the tiles as $(\mathrm{L1})_\sigma$, $(\mathrm{L2})_\sigma$, …, $(\mathrm{S3})_\sigma$ with the spin σ $(=\uparrow, \downarrow)$, which uniquely specifies spins at the corner sites. To accurately assign spins to each tile considering their vertex environments, we have considered the substitution rules under the vertex scheme. For example, as discussed above, when one applies the deflation operation to the tiling, F_0 vertices remain as F_0 vertices. Therefore the spin configuration for the tile $(\mathrm{L1})_\sigma$ and its deflation rule can be defined so that the spins at the corner sites with acute angles are not changed under the deflation operation. Then, the deflation rule for the tile $(\mathrm{L1})_\sigma$ is described as $(\mathrm{L1})_\sigma \to (\mathrm{L1})_\sigma + 2(\mathrm{P1})_\sigma + (\mathrm{S1})_\sigma$ when the spin configurations for the tiles $(\mathrm{P1})_\sigma$ and $(\mathrm{S1})_\sigma$ are defined, as shown in Fig. 2(a). In the tiling, the tile P1 always appears next to the tile L1, and we consider the substitution rule for these adjacent tiles. This gives the deflation rule for the tile $(\mathrm{P1})_\sigma$ as $(\mathrm{P1})_\sigma \to 1/2(\mathrm{L2})_\sigma + 1/2(\mathrm{L3})_\sigma + (\mathrm{P2})_\sigma$, when the spin configurations for the tiles $(\mathrm{L2})_\sigma$, $(\mathrm{L3})_\sigma$, and $(\mathrm{P2})_\sigma$ are defined, as shown in Fig. 2(a). Continuing in this fashion for the other tiles and taking into account the matching rules for the other tiles in the tiling, we therefore define the spin-dependent tiles and their

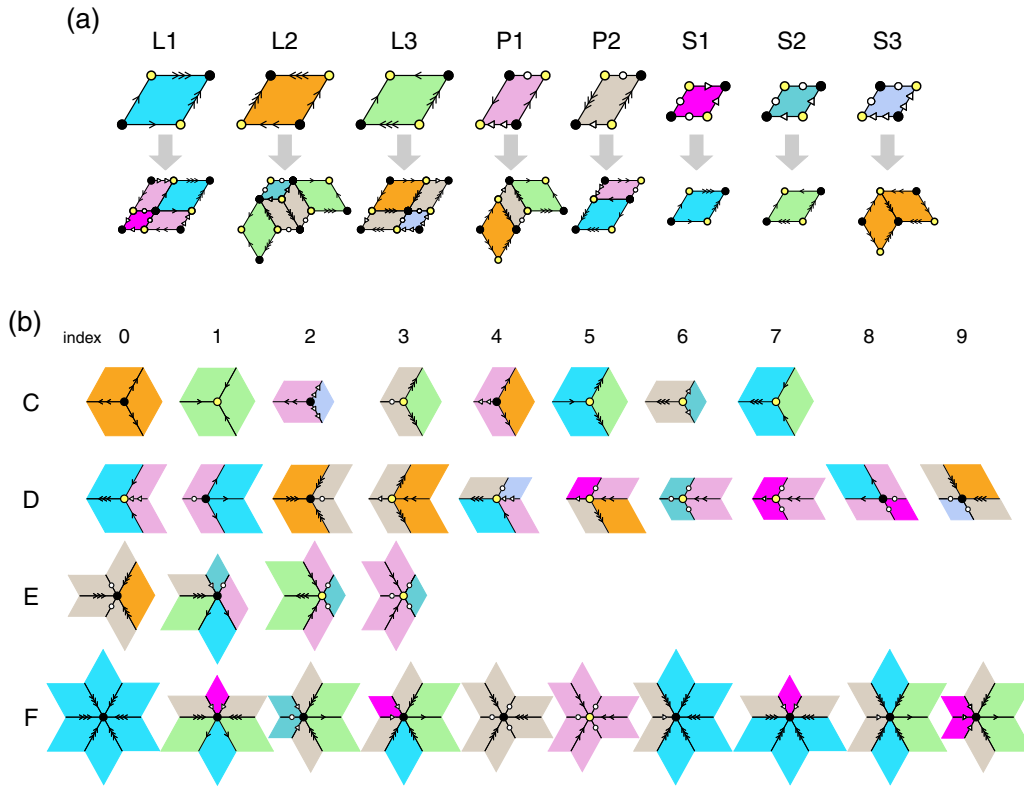

FIG. 2. (a) Inflation-deflation rule for each rhombus and parallelogram in the hexagonal golden-mean tiling [33]. Black and yellow circles at the corners indicate the "spin" (see text). Arrows, open triangles, and open circles on the edges are introduced for satisfying the matching rule in the tilings. (b) Thirty-two types of vertices in the hexagonal golden-mean tiling. Solid (open) circles at the vertices represent the sublattice A (B).

deflation rules in Fig. 2(a), where solid circles represent spin σ and open circles represent spin $\bar{\sigma}$.

To demonstrate, the number of tiles are changed under the deflation operation as $\mathbf{v}_\sigma^{n+1} = M\mathbf{v}_\sigma^n$, where $(\mathbf{v}_\sigma^n)^t = (N^n_{(\mathrm{L1})_\sigma}, N^n_{(\mathrm{L2})_\sigma}, \ldots, N^n_{(\mathrm{S3})_\sigma})$, $N^n_{\mathrm{Q}_\sigma}$ is the number of tiles Q_σ at iteration n, and

$$M = \begin{pmatrix} 1 & 0 & 0 & 0 & 1 & 1 & 0 & 0 \\ 0 & 0 & 1 & \frac{1}{2} & 0 & 0 & 0 & 1 \\ 0 & 1 & 0 & \frac{1}{2} & 0 & 0 & 1 & 0 \\ 2 & 0 & 0 & 0 & 1 & 0 & 0 & 0 \\ 0 & 2 & 2 & 1 & 0 & 0 & 0 & 0 \\ 1 & 0 & 0 & 0 & 0 & 0 & 0 & 0 \\ 0 & 1 & 0 & 0 & 0 & 0 & 0 & 0 \\ 0 & 0 & 1 & 0 & 0 & 0 & 0 & 0 \end{pmatrix}. \tag{9}$$

This transformation matrix for the number of spin-dependent tiles is diagonal with respect to the spin, implying that tiles with only one of the spins will appear in the thermodynamic limit. This property is distinct from that of the other two-dimensional quasiperiodic tilings such as the Penrose [29], Ammann-Beenker [30], and Socolar dodecagonal tilings [31], where spin-dependent tiles appear equally in the thermodynamic limit. Immediately, we find a sublattice imbalance in the vertices in the hexagonal golden-mean tiling. The 32 types of vertices are uniquely classified into two sublattices, which are shown as solid or open circles in Fig. 2(b) as a result of our spin decoration. For convenience, we refer to the sublattice which includes the F_0 vertices (solid circles) as sublattice A, and the other (open circles) as sublattice B. The fractions of sublattices A and B are obtained by

TABLE I. Fractions of C_i, D_i, E_i, and F_i vertices in the hexagonal golden-mean tiling. The asterisks indicate that the vertices are located in the B sublattice (see text).

	0	1	2	3	4	5	6	7	8	9
C	$\frac{1}{12\tau^6}$	$\frac{1}{12\tau^4}^*$	$\frac{1}{4\tau^4}$	$\frac{\sqrt{5}}{4\tau^4}^*$	$\frac{\sqrt{5}}{4\tau^4}$	$\frac{1}{4\tau^6}^*$	$\frac{1}{4\tau^4}^*$	$\frac{1}{4\tau^3}^*$		
D	$\frac{\sqrt{5}}{4\tau^4}^*$	$\frac{1}{4\tau^6}$	$\frac{1}{4\tau^6}$	$\frac{1}{4\tau^6}^*$	$\frac{1}{2\tau^4}^*$	$\frac{3}{2\tau^5}^*$	$\frac{1}{4\tau^8}^*$	$\frac{1}{4\tau^8}^*$	$\frac{1}{2\tau^4}$	$\frac{1}{4\tau^4}$
E	$\frac{\sqrt{5}}{4\tau^6}$	$\frac{\sqrt{5}}{2\tau^6}$	$\frac{1}{4\tau^6}^*$	$\frac{\sqrt{5}}{4\tau^8}^*$						
F	$\frac{1}{4\tau^6}$	$\frac{1}{2\tau^6}$	$\frac{1}{4\tau^8}$	$\frac{\sqrt{5}}{2\tau^8}$	$\frac{1}{12\tau^8}$	$\frac{1}{12\tau^{10}}^*$	$\frac{\sqrt{5}}{4\tau^8}$	$\frac{1}{2\tau^8}$	$\frac{1}{4\tau^{10}}$	$\frac{1}{4\tau^8}$

summing the relevant terms of Table I as $f_A = 1/2 - \sqrt{5}/(12\tau^3)$ and $f_B = 1/2 + \sqrt{5}/(12\tau^3)$. Then, the sublattice imbalance is given as

$$|f_A - f_B| = \frac{\sqrt{5}}{6\tau^3} \sim 0.088. \tag{10}$$

We note that the sublattice imbalance originates inherently from the structure of the hexagonal golden-mean tiling. Therefore the sublattice imbalance is represented by an irrational number, which is distinct from the trivial case in bipartite decorated lattices, for example, the Lieb lattice with $|f_A - f_B| = 1/3$. In the following, we omit the spin index in the tiles and vertices to discuss magnetic properties in the correlated electron system on the hexagonal golden-mean tiling.

III. MODEL AND HAMILTONIAN

We study the Hubbard model on the hexagonal golden-mean tiling, which is given by the following Hamiltonian:

$$H = -t \sum_{(ij),\sigma} (c^\dagger_{i\sigma} c_{j\sigma} + \text{H.c.}) + U \sum_i n_{i\uparrow} n_{i\downarrow}, \tag{11}$$

where $c_{i\sigma}$ ($c^\dagger_{i\sigma}$) annihilates (creates) an electron with spin σ ($=\uparrow, \downarrow$) at the ith site and $n_{i\sigma} = c^\dagger_{i\sigma} c_{i\sigma}$. t denotes the nearest-neighbor transfer integral, and U denotes the on-site Coulomb interaction. For simplicity, we have assumed that the magnitude of the hopping integral is uniform in the system. The chemical potential is always $\mu = U/2$ when the electron density is fixed to be half filling. According to Lieb's theorem [34], the half-filled Hubbard model on the bipartite lattice has a ground state with total spin $S_{\text{tot}} = \frac{1}{2}|N_A - N_B|$. In fact, it has been clarified that the magnetically ordered states with finite total spin are realized in some periodic Hubbard systems [34–40]. As we have discussed, the vertex model on the hexagonal golden-mean tiling has a sublattice imbalance, so that the magnetically ordered state is realized with a total spin $\sqrt{5}/(12\tau^3) \times N$, where N ($= N_A + N_B$) is the total number of sites.

To discuss magnetic properties in the Hubbard model, we make use of the real-space mean-field theory. This method has an advantage in treating large clusters, which is crucial to clarifying magnetic properties in the system with a quasiperiodic tiling. Here, we introduce the site-dependent mean-field $\langle n_{i\sigma} \rangle$. The mean-field Hamiltonian is then given as

$$H^{\text{MF}} = -t \sum_{(ij),\sigma} (c^\dagger_{i\sigma} c_{j\sigma} + \text{H.c.}) + U \sum_{i,\sigma} n_{i\sigma} \langle n_{i\bar{\sigma}} \rangle. \tag{12}$$

For given values of $\langle n_{i\sigma} \rangle$, we numerically diagonalize the Hamiltonian H^{MF}, update $\langle n_{i\sigma} \rangle$, and repeat this procedure until the result converges. The uniform and staggered magnetizations $m^\pm$ are given as

$$m^\pm = f_A m_A \pm f_B m_B, \tag{13}$$

$$m_\alpha = \frac{1}{N_\alpha} \sum_{i \in \alpha} m_i, \tag{14}$$

$$m_i = \tfrac{1}{2}(\langle n_{i\uparrow} \rangle - \langle n_{i\downarrow} \rangle), \tag{15}$$

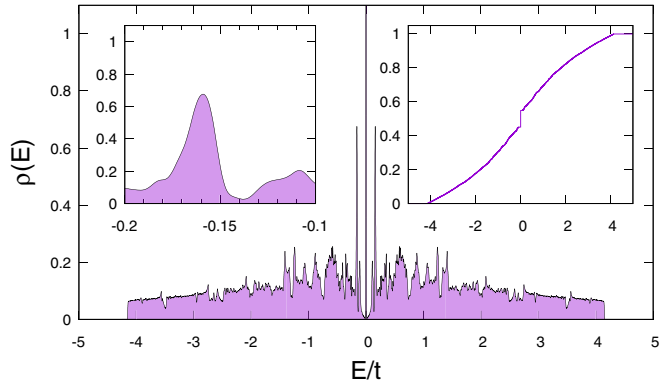

FIG. 3. Density of states of the tight-binding model on the hexagonal golden-mean tiling with $N = 1\,172\,071$. The left inset shows the magnified figure around $E = -0.16t$, and the right inset shows the integrated density of states.

where N_α (m_α) is the number of sites (average of the magnetization) in the sublattice α ($= A, B$) and m_i is the magnetization at the ith site.

When the system is noninteracting ($U = 0$), the model Hamiltonian is reduced to the tight-binding model. Diagonalizing the Hamiltonian for the system with $N = 1\,172\,071$, we obtain the density of states, which is defined as

$$\rho(E) = \frac{1}{N} \sum_i \delta(E - \epsilon_i), \tag{16}$$

where ϵ_i is the eigenenergy. The results are shown in Fig. 3, which is symmetric since the system is bipartite. We also find the delta-function peak at $E = 0$, which implies the existence of macroscopically degenerate states. These confined states should be important for magnetic properties in the weak coupling limit and are features common to bipartite quasiperiodic tilings. In addition, we find sharp peaks at $E/t \sim \pm 0.16$, but these have small widths, so that the corresponding eigenstates are not strictly localized in a certain region in contrast to the confined states with $E = 0$.

IV. CONFINED STATES

Here, we study the confined states in detail; since the confined states with $E = 0$ are macroscopically degenerate, we can choose a simple form by considering their linear combinations, as discussed in several papers [29,41,42]. It is known that six types of the confined state appear in the Penrose case [29,42], while in the Ammann-Beenker and Socolar dodecagonal cases, the number of types is infinite [30,31]. In the hexagonal golden-mean tiling, infinite types of confined states should appear, similar to the latter two tilings. Some simple examples of confined states around the F_0 vertices are explicitly shown in Fig. 4, labeled as $\Psi_1, \ldots, \Psi_5$. We find two confined states, Ψ_1 and Ψ_2, in the smallest region with sixfold rotational symmetry. The amplitudes in Ψ_1 appear at the F_0 vertex and next-nearest neighbor C_6 and D_8 vertices in sublattice A. By contrast, the amplitudes in Ψ_2 appear at the D_5 vertices in sublattice B. Since the confined states have amplitudes in both sublattices, we can say that the introduction of the Coulomb interaction lifts the degeneracy at

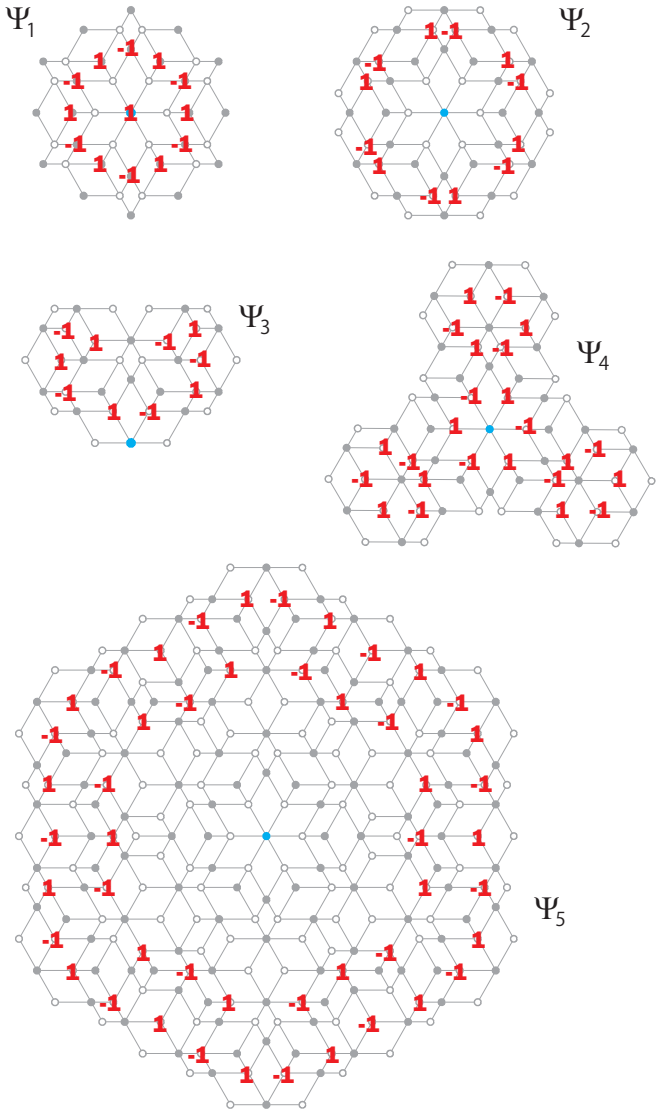

FIG. 4. Five confined states around the F_0 vertex (blue points). Solid (open) circles represent the sublattice A (B). The numbers at the vertices represent the amplitudes of the confined states.

$E = 0$, stabilizing the magnetically ordered state with a finite staggered magnetization. We note that these confined states do not necessarily exist around all the F_0 vertices. In fact, each fraction (Ψ_1, Ψ_2) is given as $1/(4\tau^8)$ (smaller than f_{F_0}). The fractions of the other examples of confined states Ψ_3, Ψ_4, and Ψ_5 are given by $5/(4\tau^{10})$, $2/(4\tau^{10})$, and $1/(4\tau^{12})$, by taking each local symmetry into account. Away from the F_0 vertices, Figure 5 shows five examples of confined states around different vertices. Wave functions Φ_1 and Φ_4 are located around the F_4 and C_0 vertices, respectively, which exhibit threefold rotational symmetry, while Φ_2, Φ_3, and Φ_5 are located at vertices which locally have no rotational symmetry. As seen in Figs. 4 and 5, many kinds of confined states are expected in the thermodynamic limit. Therefore we cannot count the number of confined states systematically, in contrast to the Ammann-Beenker tiling, for example.

We wish to note that the confined states having amplitudes in sublattice A should be restricted to Ψ_1, as shown in Figs. 4 and 5. We cannot prove this analytically, but rather confirm it numerically in a cluster with $N = 448\,213$, which will be shown later. This conjecture immediately gives us the lower bound of the fraction of the confined states, by considering magnetic properties in the weak coupling limit. In the limit, the confined states play an essential role for magnetic properties, and the uniform magnetization is given as $m^+ = (f_A^C - f_B^C)/2$, where f_A^C (f_B^C) is the fraction of the confined states in sublattice A (B). Namely, as before, $f_A^C = 1/(4\tau^8)$. The uniform magnetization is directly related to the sublattice imbalance equation (10). As such, we obtain the fraction of the confined states as

$$f^C = f_A^C + f_B^C = \frac{\tau + 9}{6\tau^6} \sim 0.0986. \tag{17}$$

This value is conjectured to be an exact fraction and is consistent with the numerical results $f^C = 0.098\,168$ for a cluster with $N = 835\,393$, where the eigenstates with $E = 0$ around the edge are excluded.

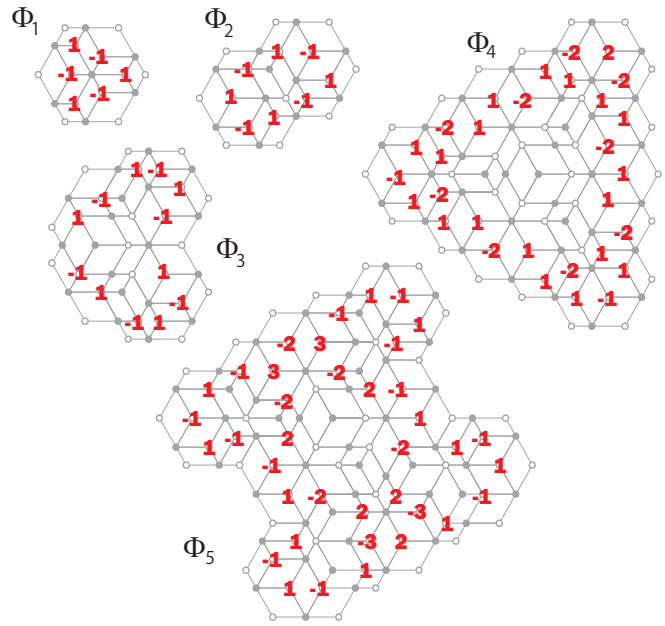

FIG. 5. Five confined states. Solid (open) circles represent sublattice A (B). The numbers at the vertices represent the amplitudes of the confined states.

V. MAGNETIC PROPERTIES

In the following, we discuss magnetic properties in the Hubbard model on the hexagonal golden-mean tiling. We mainly treat the system with $N = 448\,213$ by means of the real-space mean-field approximations. When the system is noninteracting, the macroscopically degenerate states in the density of states appear at the Fermi level, as shown in Fig. 3. The introduction of the interaction lifts the degeneracy, stabilizing the magnetically ordered state. The magnetization profile for the case with $U/t = 1.0 \times 10^{-6}$ is shown in Fig. 6(a). We find finite magnetizations at certain sites, which reflects the spatial distribution of the confined states. We note that in sublattice A, finite magnetization only appears at the F_0 vertices and their next-nearest-neighbor C_4 and D_8 vertices

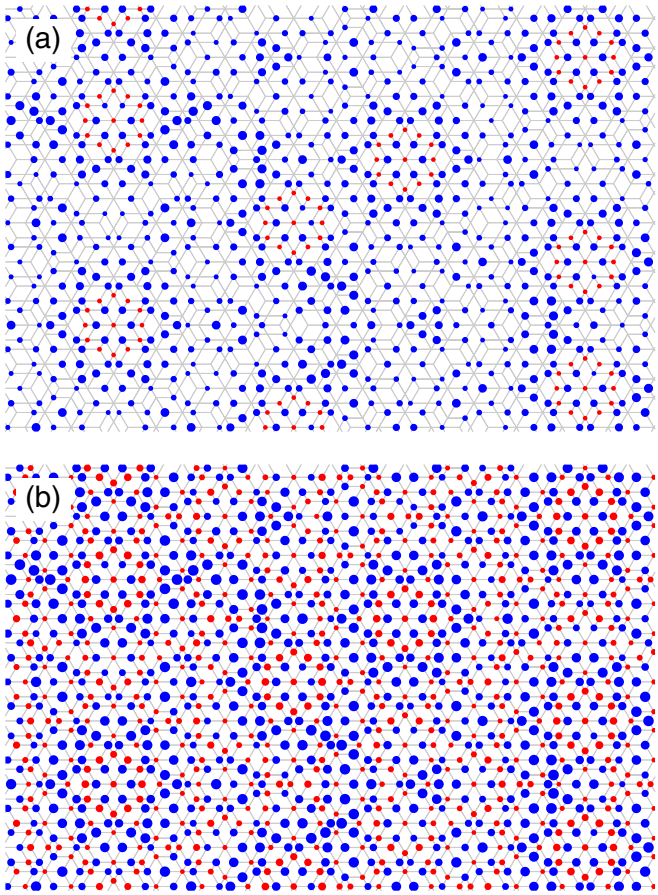

FIG. 6. Spatial pattern for the staggered magnetizations in the Hubbard model on the hexagonal golden-mean tiling when (a) $U/t = 1.0 \times 10^{-6}$ (essentially the same as $U \to 0$) and (b) $U/t = 1$. The area of the circles represents the magnitude of the local magnetization.

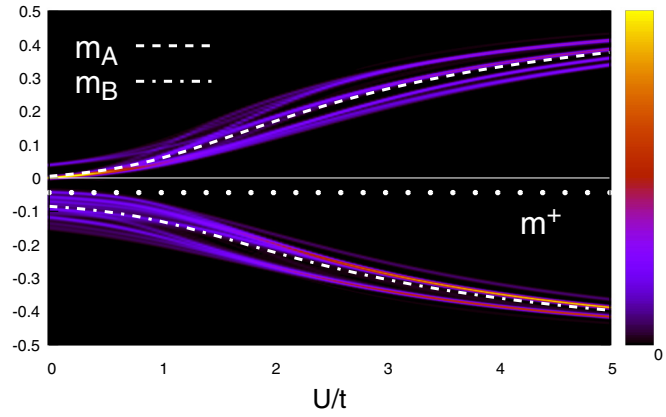

FIG. 7. Distribution of the local magnetizations as a function of U/t in the system with $N = 448\,213$. The dashed (dot-dashed) line represents the magnetization m_A (m_B), and the dotted line represents the total uniform magnetization.

(shown in red). This is consistent with the fact that in sublattice A, Ψ_1 is the only type of confined state. Therefore the magnetization at these vertices takes $m_i = 1/26$. In contrast, each site on sublattice B has a local magnetization, as shown by the blue circles in Fig. 6(a), where the area of the circles represents the magnitude of the local magnetization. This implies that at each site in sublattice B, some confined states have amplitudes. For this reason, nonmagnetic sites only belong to sublattice A, and their fraction should be given as $f_{\rm non} = f_A - 13 f_A^C \sim 0.387$. Imbalanced magnetic properties in the weak coupling limit are distinct from those for the quasiperiodic tilings such as Penrose, Ammann-Beenker, and Socolar dodecagonal tilings [29–31]. Namely, the averages of the total uniform and staggered magnetizations are given as $|m^+| = 0.044$ and $|m^-| = 0.049$.

When we increase the interaction strength, the absolute value of the magnetization at each site monotonically increases, and the nonmagnetic sites now have positive magnetizations, as shown in Fig. 6(b). The distribution of the local magnetization is shown in Fig. 7. When $U/t \leqslant 1$, the distribution is similar to that in the weak coupling limit $U/t \to 0$, where a sharp peak appears in the case $m > 0$ (sublattice A), while a broader structure appears in the case $m < 0$ (sublattice B). In contrast, when $U/t \geqslant 2$, distinct behavior appears in the magnetic distribution. In this case, the absolute values of the local magnetization should be classified into four groups, specified by the coordination number of the vertices—although two of the four may be invisible in the case $m < 0$. The crossover between weak and strong coupling regimes occurs around $U/t \sim 1.5$. In the strong coupling limit $U/t \to \infty$, the Hubbard model is reduced to the antiferromagnetic Heisenberg model with nearest-neighbor couplings $J = 4t^2/U$. The mean-field ground state is then described by the staggered moment $m_j = \pm 1/2$. This means that the mean-field approach cannot correctly describe the reduction of the magnetic moment due to quantum fluctuations. Therefore an elaborate method is necessary to precisely clarify magnetic properties in this regime, which is beyond the scope of the present study. Nevertheless, interesting magnetic properties inherent in the hexagonal golden-mean tiling can be captured correctly, even in our simple mean-field method; note that the total uniform magnetization is never changed, which is consistent with Lieb's theorem [34].

Finally, we wish to demonstrate the spatial profile of the magnetizations characteristic of the hexagonal golden-mean tiling. To this end, we map it to the perpendicular space, where the positions in perpendicular space have one-to-one correspondence with the positions in the physical space. Each site in the tiling is described by a six-dimensional lattice point $\vec{n} = (n_0, n_1, \ldots, n_5)$, labeled with integers n_m, where the lattice is spanned by fundamental translation vectors. The coordinates of the tiling are the projections onto the two-dimensional physical space:

$$\mathbf{r} = (x, y) = \sum_{m=0}^{5} n_m \mathbf{e}_m, \tag{18}$$

where $\mathbf{e}_m$ are the projected vectors and are given as $= \tau(\cos(-2/3\pi m), \sin(-2/3\pi m))$ for $m = 0, 1, 2$ and $\mathbf{e}_m = (\cos(-2/3\pi m), \sin(-2/3\pi m))$ for $m = 3, 4, 5$, shown in Fig. 1(b). We can then project the points onto the four-dimensional perpendicular space (split into 2 two-dimensional

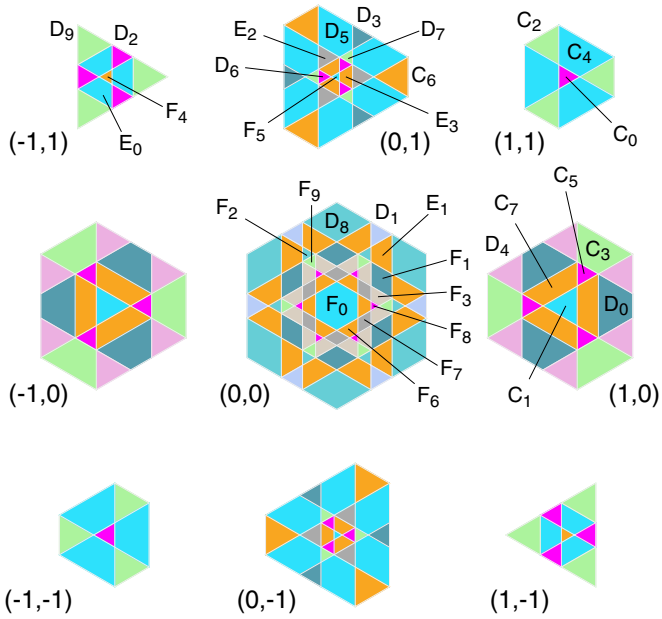

FIG. 8. Perpendicular spaces $\mathbf{r}^{\perp}$ for the hexagonal golden-mean tiling. Each area bounded by the solid lines is the region of one of 32 types of vertices shown in Fig. 2(b).

spaces $\tilde{\mathbf{r}}$ and $\mathbf{r}^{\perp}$), giving information specifying the local environment of each site:

$$\tilde{\mathbf{r}} = \sum_{m=0}^{5} n_m \tilde{\mathbf{e}}_m, \tag{19}$$

$$\mathbf{r}^{\perp} = \sum_{m=0}^{5} n_m \mathbf{e}_m^{\perp}, \tag{20}$$

where $\tilde{\mathbf{e}}_m = \mathbf{e}_{m+3}$ for $m = 0, 1, 2$ and $\tilde{\mathbf{e}}_m = -\mathbf{e}_{m-3}$ for $m = 3, 4, 5$. $\mathbf{e}^{\perp} = (1, 0)$ for $m = 0, 1, 2$, and $\mathbf{e}^{\perp} = (0, 1)$ for $m = 3, 4, 5$. In the hexagonal golden-mean tiling, $\mathbf{r}^{\perp} = (x^{\perp}, y^{\perp})$ takes nine values $x^{\perp} = -1, 0, 1$ and $y^{\perp} = -1, 0, 1$. In each $\mathbf{r}^{\perp}$ plane, the $\tilde{\mathbf{r}}$ points densely cover a certain region. Moreover, the region in plane $\mathbf{r}^{\perp}$ has the same size as the one in the plane $(-\mathbf{r}^{\perp})$. Figure 8 shows the perpendicular space for the system. The plane (0,0) has sixfold rotational symmetry, while the others have threefold rotational symmetry. We have previously shown that the 32 types of vertices are mapped into specific regions in certain planes [33]. This implies that the perpendicular space reflects the local environments for the lattice sites, such that the areas of each vertex region in perpendicular space are proportional to its fraction in parallel space. As such, we also find that the vertices in sublattice A (B) are mapped to the planes with (0,0), $(\pm 1, \pm 1)$, and $(\pm 1, \pm 1)$ [$(0, \pm 1)$ and $(\pm 1, 0)$]. This can be explained by the following: The sublattice index for each vertex is uniquely determined, as discussed above. Since upon moving from one site to its neighbor only one of the n_m's changes by ± 1, an even (odd) number $(x^{\perp} + y^{\perp})$ corresponds to sublattice A (B). Correspondingly, the areas for both sublattices are different from each other, which is consistent with the existence of the sublattice imbalance.

The magnetization profile in perpendicular space is shown in Fig. 9, where we have shown the absolute values of the local magnetizations. When $U/t = 1.0 \times 10^{-6}$, the finite magnetization appears in the whole of the planes $(0, \pm 1)$ and $(\pm 1, 0)$, implying that the local magnetizations appear in sublattice B. In contrast, in sublattice A, finite magnetization appears only in specific hexagonal regions in three planes: $(-1, -1)$, (0,0), and (1, 1). This is consistent with the fact that only the confined states Ψ_1 with amplitudes at C_4, D_8, and F_0 vertices are magnetized. Upon increasing the interaction strength, all vertex sites are magnetized, as shown in Fig. 9(b). When $U/t = 5$, the local magnetization takes large values. An important point is that the magnetization profile in each plane is different from that for the weak coupling case. In the weak coupling case, the magnetization profile originates from the spatial distribution of the confined states. On the other hand, in the strong coupling case, the Coulomb interactions play a crucial role in stabilizing the ferrimagnetically ordered states, where intersite correlations become important. In fact, the magnitude of local magnetizations can be classified into four groups specified by the coordination number, as shown in Fig. 9(c) by the four separate groups of color contrast regions.

Before concluding, we would like to comment on and compare the magnetic properties derived in the Hubbard model on the Penrose, Ammann-Beenker, Socolar dodecagonal, and hexagonal golden-mean tilings. One of the common features across these tilings is the existence of confined states at $E = 0$ in the noninteracting case ($U = 0$), which play a crucial role in stabilizing the magnetically ordered states in the weak coupling limit. Nevertheless, their confined state properties are distinct from each other. As for the number of types of confined states, it is restricted to be 6 in the Penrose case [41,42], while it should be infinite in the others. The sublattice imbalance appears only in the hexagonal golden-mean tiling, uniquely leading to a ferrimagnetically ordered state. In contrast, for the other tilings, antiferromagnetically ordered states are realized without spontaneous uniform magnetization.

VI. SUMMARY

We have studied the magnetic properties in the half-filled Hubbard model on the hexagonal golden-mean tiling. Examining the lattice structure, we have found that the vertex model is bipartite, with a sublattice imbalance of $\sqrt{5}/(6\tau^3)$. We have found the delta-function peak in the density of states of the tight-binding model, implying the existence of macroscopically degenerate confined states at $E = 0$. We have then clarified that one type of the confined states has amplitudes in sublattice A, while the others are only in sublattice B. These facts give us the lower bound on the fraction of the confined states as $(\tau + 9)/(6\tau^6) \sim 0.0986$, which is conjectured to be the exact fraction. Furthermore, these findings lead to a ferrimagnetically ordered state even in the weak coupling limit. Then, the introduction of the Coulomb interaction lifts the macroscopic degeneracy at the Fermi level and induces the finite staggered magnetization as well as uniform magnetization. By applying the real-space mean-field approach to the Hubbard model, we have clarified how the spatial distribution of the magnetizations continuously changes with

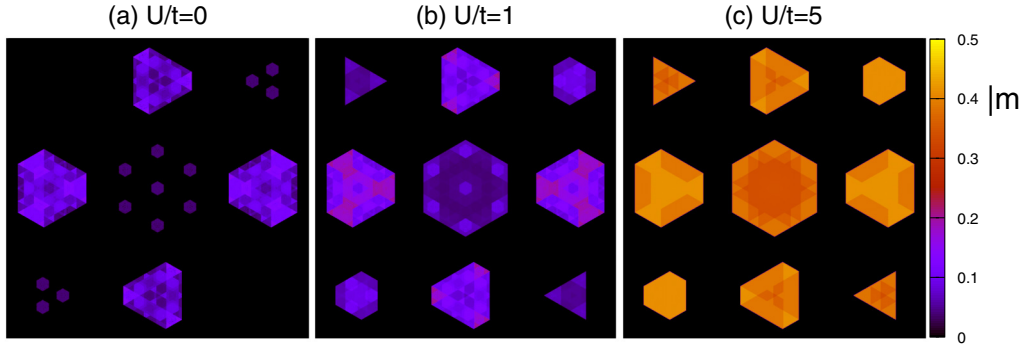

FIG. 9. Magnetization profile in the perpendicular space $(\tilde{x}, \tilde{y})$ for the Hubbard model with $N = 448\,213$ when (a) $U/t = 1.0 \times 10^{-6}$, (b) $U/t = 1$, and (c) $U/t = 5$.

increasing interaction strength. The crossover behavior in the magnetically ordered states has been discussed, by applying the perpendicular space analysis to the local magnetizations. It is also interesting to clarify how the ferrimagnetically ordered state competes with the paramagnetic metal, ferromagnetically ordered state, and phase separation away from the half filling, which is now under consideration.

ACKNOWLEDGMENTS

Parts of the numerical calculations are performed in the supercomputing systems in ISSP, The University of Tokyo. This work was supported by Grant-in-Aid for Scientific Research from JSPS, KAKENHI Grants No. JP19H05821, No. JP18K04678, and No. JP17K05536 (A.K.) and No. JP19H05817 and No. JP19H05818 (S.C.).

[1] D. Shechtman, I. Blech, D. Gratias, and J. W. Cahn, Phys. Rev. Lett. **53**, 1951 (1984).
[2] T. Ishimasa, Y. Tanaka, and S. Kashimoto, Philos. Mag. **91**, 4218 (2011).
[3] K. Deguchi, S. Matsukawa, N. K. Sato, T. Hattori, K. Ishida, H. Takakura, and T. Ishimasa, Nat. Mater. **11**, 1013 (2012).
[4] K. Kamiya, T. Takeuchi, N. Kabeya, N. Wada, T. Ishimasa, A. Ochiai, K. Deguchi, K. Imura, and N. K. Sato, Nat. Commun. **9**, 154 (2018).
[5] K. Kimura, T. Hashimoto, K. Suzuki, K. Nagayama, H. Ino, and S. Takeuchi, J. Phys. Soc. Jpn. **55**, 534 (1986).
[6] J. J. Hauser, H. S. Chen, and J. V. Waszczak, Phys. Rev. B **33**, 3577 (1986).
[7] K. Fukamichi, T. Goto, T. Masumoto, T. Sakakibara, M. Oguchi, and S. Todo, J. Phys. F: Met. Phys. **17**, 743 (1987).
[8] C. H. Chen and H. S. Chen, Phys. Rev. B **33**, 2814 (1986).
[9] A.-P. Tsai, A. Inoue, T. Masumoto, and N. Kataoka, Jpn. J. Appl. Phys. **27**, L2252 (1988).
[10] M. F. Hundley, M. E. Mchenry, R. A. Dunlap, V. Srinivas, and D. Bahadur, Philos. Mag. B **66**, 239 (1992).
[11] Y. Hattori, A. Niikura, A. P. Tsai, A. Inoue, T. Masumoto, K. Fukamichi, H. Aruga-Katori, and T. Goto, J. Phys.: Condens. Matter **7**, 2313 (1995).
[12] B. Charrier and D. Schmitt, J. Magn. Magn. Mater. **171**, 106 (1997).
[13] T. J. Sato, H. Takakura, A. P. Tsai, and K. Shibata, Phys. Rev. Lett. **81**, 2364 (1998).
[14] T. J. Sato, J. Guo, and A. P. Tsai, J. Phys.: Condens. Matter **13**, L105 (2001).
[15] R. Tamura, Y. Muro, T. Hiroto, K. Nishimoto, and T. Takabatake, Phys. Rev. B **82**, 220201(R) (2010).
[16] R. Tamura, A. Ishikawa, S. Suzuki, T. Kotajima, Y. Tanaka, T. Seki, N. Shibata, T. Yamada, T. Fujii, C.-W. Wang, M. Avdeev, K. Nawa, D. Okuyama, and T. J. Sato, J. Am. Chem. Soc. **143**, 19938 (2021).
[17] N. Takemori and A. Koga, J. Phys. Soc. Jpn. **84**, 023701 (2015).
[18] S. Takemura, N. Takemori, and A. Koga, Phys. Rev. B **91**, 165114 (2015).
[19] R. Shinzaki, J. Nasu, and A. Koga, J. Phys. Soc. Jpn. **85**, 114706 (2016).
[20] J. B. Hauck, C. Honerkamp, S. Achilles, and D. M. Kennes, Phys. Rev. Research **3**, 023180 (2021).
[21] S. Sakai, N. Takemori, A. Koga, and R. Arita, Phys. Rev. B **95**, 024509 (2017).
[22] S. Sakai and R. Arita, Phys. Rev. Research **1**, 022002(R) (2019).
[23] K. Inayoshi, Y. Murakami, and A. Koga, J. Phys. Soc. Jpn. **89**, 064002 (2020).
[24] Y. Cao, Y. Zhang, Y.-B. Liu, C.-C. Liu, W.-Q. Chen, and F. Yang, Phys. Rev. Lett. **125**, 017002 (2020).
[25] N. Takemori, R. Arita, and S. Sakai, Phys. Rev. B **102**, 115108 (2020).
[26] S. Wessel, A. Jagannathan, and S. Haas, Phys. Rev. Lett. **90**, 177205 (2003).
[27] A. Jagannathan, A. Szallas, S. Wessel, and M. Duneau, Phys. Rev. B **75**, 212407 (2007).
[28] A. Jagannathan and H. J. Schulz, Phys. Rev. B **55**, 8045 (1997).
[29] A. Koga and H. Tsunetsugu, Phys. Rev. B **96**, 214402 (2017).
[30] A. Koga, Phys. Rev. B **102**, 115125 (2020).
[31] A. Koga, Mater. Trans. **62**, 360 (2021).
[32] S. Sakai and A. Koga, Mater. Trans. **62**, 380 (2021).
[33] S. Coates, R. Lifshitz, A. Koga, R. McGrath, H. R. Sharma, and R. Tamura, arXiv:2201.11848 [cond-mat.soft].

[34] E. H. Lieb, Phys. Rev. Lett. **62**, 1201 (1989).
[35] A. Mielke, J. Phys. A: Math. Gen. **25**, 4335 (1992).
[36] H. Tasaki, Phys. Rev. Lett. **69**, 1608 (1992).
[37] K. Kusakabe and H. Aoki, J. Phys. Soc. Jpn. **61**, 1165 (1992).
[38] A. M. S. Macédo, M. C. dos Santos, M. D. Coutinho-Filho, and C. A. Macédo, Phys. Rev. Lett. **74**, 1851 (1995).
[39] G.-S. Tian and T.-H. Lin, Phys. Rev. B **53**, 8196 (1996).
[40] K. Noda, A. Koga, N. Kawakami, and T. Pruschke, Phys. Rev. A **80**, 063622 (2009).
[41] M. Kohmoto and B. Sutherland, Phys. Rev. Lett. **56**, 2740 (1986).
[42] M. Arai, T. Tokihiro, T. Fujiwara, and M. Kohmoto, Phys. Rev. B **38**, 1621 (1988).